

FERARI and cargo adaptors coordinate cargo flow through sorting endosomes

Jachen Solinger

University of Basel

Harun-Or Rashid

University of Basel

Anne Spang (✉ anne.spang@unibas.ch)

University of Basel <https://orcid.org/0000-0002-2387-6203>

Article

Keywords: tether, recycling endosomes, endocytosis, *C. elegans*, small GTPases, SM protein, SNAREs, vesicle transport, Rab proteins, mammalian cells, CRISPR, membrane fusion, membrane fission, adaptor proteins

DOI: <https://doi.org/10.21203/rs.3.rs-701696/v1>

License: © ⓘ This work is licensed under a Creative Commons Attribution 4.0 International License.

[Read Full License](#)

Abstract

Cellular organization, compartmentalization and cell-to-cell communication are crucially dependent on endosomal pathways. Sorting endosomes provide a transit point for various trafficking pathways and decide the fate of proteins: recycling, secretion or degradation. FERARI (Factors for Endosome Recycling and Rab Interactions) plays a key role in shaping these compartments and coordinates Rab GTPase function with membrane fusion and fission of vesicles through a kiss-and-run mechanism. Here we show that cargo concentration in sorting endosomes determines the length of the kiss between Rab11 and SNX1 structures, presumably by clogging the fusion stalk. Cargo flow from sorting endosomes into Rab11 structures relies on the cargo adaptor SNX6, while cargo retention in the Rab11 endosome is dependent on AP1. Similar to Rab11, Rab5 and Rab10 positive endosomes also interact with the SNX1 tubular network through FERARI-dependent kiss-and-run. We propose that FERARI, together with cargo adaptors, coordinates the vectorial flow of cargo through sorting endosomes.

Introduction

Cells are constantly interacting and exchanging materials and signals with their surroundings. To accomplish this, they need to have efficient machineries for uptake and recycling of proteins and solutes. While the uptake of cargo through endocytosis has been extensively studied and is quite well understood, the recycling and sorting part of the cycle is less clear^{1,2}. Many factors involved in endosomal sorting and recycling have been described³, and microscopic analyses revealed a fascinating and complex network of dynamic tubules, where these processes take place⁴. Current models concentrate on early sorting events occurring directly at Rab5-positive structures⁵. Sorting nexins (SNXs) with membrane tubulation activities form tubules, where adaptor proteins are recruited and attract cargo. These transport carriers acquire the appropriate Rab GTPase (e.g. Rab11) and will be pinched off to form vesicles with defined cargoes, which can be transported to their final destination. These transport routes use retromer and retriever complexes for the transport of many different cargoes⁶. While this model addresses many features of cargo sorting and recycling, it falls short to explain the presence of large tubular recycling networks or how low binding affinities of cargo adaptors can ensure efficient separation and sorting of cargoes. We recently described an additional mechanism by which cargo sorting might occur at sorting endosomes. In this process, FERARI promotes a kiss-and-run between Rab11 positive recycling vesicles and the tubular SNX1 sorting endosomes⁷. FERARI contains proteins for tethering (Rab11FIP5, Rabenosyn 5), SNARE interactions (VPS45), binding to SNXs (VIPAS39), scaffolding and protein-protein interactions (ANK1) as well as membrane tubule stabilization and pinching (EHD1)⁷. The integration of all these factors for recycling into one machinery allows for a tightly regulated mechanism of tethering, docking, cargo exchange and fission of vesicles. However, more studies are needed to fully understand the process of cargo sorting in endosome recycling.

In this study, we find that the length of the kiss between the recycling and the sorting endosome correlates with cargo concentration in the sorting endosome. Moreover, the cargo adaptor SNX6 on

sorting endosomes regulates the flow of cargo into the recycling endosome. Unexpectedly, Rab5 and Rab10 positive endosomes also undergo FERARI mediated kiss-and run at SNX1 endosomes with similar kinetics than Rab11 positive structures. Our data are consistent with a model in which cargo flows from Rab5 positive early endosomes through the SNX1 sorting compartment into Rab11 recycling endosomes. In this model, Hrs/ESCRT-0 appears to retain cargo in the Rab5 endosomes that should be going into the degradative pathway, while the rest of the cargoes could reach SNX1 positive tubules, from which they can reach recycling endosomes. Adaptor complex 1 (AP1) would prevent cargo from diffusing back from recycling into sorting endosomes. Therefore, interactions between cargoes and their adaptors control their vectorial flow from early to recycling endosomes.

Results

Cargo amount determines length of the kiss between RAB-11 and SNX-1 compartments.

We noticed previously that cargo vesicles containing hTfR-GFP or Glut1-GFP showed extended residence times on SNX-1 compartments compared to RAB-11 vesicles, even though these cargoes would leave the SNX-1 compartment in RAB-11 vesicles⁷. We hypothesized that cargo concentration may influence the length of the residence time (kiss). To test this hypothesis, we reduced cargo availability by downregulating hTfR-GFP and Glut1-GFP levels using RNAi against GFP (Fig. S1 A-D). The length of the kiss of hTfR-GFP and Glut1-GFP vesicles was reduced and was comparable to the residence times that we had observed previously for RAB-11, but the 7 sec periodicity was not perturbed by the reduced cargo levels (Fig. 1A and B, Fig. S1E-H,⁷).

Next, we asked how cargo availability would influence the Rab11 residence time. We hypothesized that high cargo concentrations might cause cargo to become stuck in the fusion pore or the stalk. To gain better understanding, we first built a model based on the stalk diameters to which EHD proteins would bind and the size of hTfR⁸⁻¹¹ (Fig. 1C). In addition, cargo would prefer regions of negative membrane curvature^{12,13}. Therefore, cargo might potentially obstruct the stalk between recycling and sorting endosomes. We envisage the 7s intervals to be the time for an attempted fission event, which is abortive when cargo is still present in the stalk. In a nutshell, cargo in the stalk would prevent membrane fission. We next went on to test our model.

SNX-6 is involved in the regulation of the length of the kiss between RAB-11 and SNX-1 compartments

To ensure proper cargo sorting into the RAB-11 recycling compartment, regulation of cargo flow is required. In fact, cargo sorting in the sorting compartment is supposed to be regulated by multiple cargo adaptors^{6,14}. Mammalian cargo adaptors SNX5 and SNX6 interact with SNX1¹⁵, making them prime

candidates as potential regulators of cargo sorting. To interfere with sorting into RAB-11 vesicles in *C. elegans*, we knocked down SNX-6, the sole homolog of mammalian SNX5/6. The result of the knockdown was threefold. First, we found that at least some of the Rab11 vesicles that would normally just kiss-and-run must have fused with membrane flattening yielding RAB-11 patches on the SNX-1 network, as highlighted by an increase in the Mander's coefficients (Fig. 1D, movie 1). Second, the RAB-11 vesicles that underwent kiss-and-run stayed there for long times (Fig. 1E, Fig. S2A). Third, the RAB-11 vesicles were smaller in *snx-6(RNAi)* than in control animals (Fig. 1F, Fig. S2E). All three effects are consistent with a defect in cargo sorting. In the absence of SNX-6, cargo fails to be sorted into the recycling vesicles, but instead cargo could diffuse into the neck and interfere with fusion pore closure thereby extending the docked stage between RAB-11 and SNX-1 compartments. Since the cargo flux into RAB-11 vesicles would be suboptimal, they would eventually leave with little cargo resulting in smaller vesicles. This effect might be aggravated by potentially reduced cargo availability in *snx-6(RNAi)* sorting compartments due to reduced recruitment of cargo into tubular sorting structures (see also below). Taken together, our results so far indicate that cargo amounts and cargo flow regulated by SNX-6 directly affect kiss-and-run and thereby most likely also FERARI function.

Kiss-and-run between Rab11 and SNX1 compartments are conserved in mammalian cells

While we have previously shown that FERARI is conserved in metazoan and our data were also consistent with a functional conservation, we had not shown that FERARI-dependent kiss-and-run of Rab11 vesicles on SNX1 sorting endosomes occurred. Therefore, we imaged HeLa cells expressing GFP-Rab11 and mCherry-SNX1. Indeed, we observed kiss-and-run events with a similar quantal behavior as in *C. elegans*⁷ (Fig. 1G and H, movie 2), with the sole difference that the residence times increased with a 4-sec periodicity, compared to 7 sec in *C. elegans*. This difference in the periodicity might be due to the temperature difference at which these events were measured; 37°C for mammalian cells and 20°C for worms. Nevertheless, like in *C. elegans*, these kiss-and-run events required FERARI function, as knockout lines of FERARI abolished kiss-and-run between Rab11 and SNX1 compartments (Fig. 1G and H, Fig. S1K, Fig. S3A, movie 2). We conclude the function of FERARI is conserved from *C. elegans* to mammals.

SNX5/6 are involved in Rab11-dependent recycling

Next, we tested whether the sorting defects caused by *snx-6(RNAi)* in *C. elegans* were conserved in mammalian cells. We knocked out SNX5 and SNX6 in HeLa cells (Fig. S4C) and assessed the co-localization of Rab11 and SNX1. Surprisingly, we observed a reduction in the co-localization between Rab11 and Snx1 in *snx5/6* KO cells (Fig. 2A and B). In part, this decrease in co-localization might be explained by the reduced stability of SNX1 upon loss of SNX5 and SNX6, presumably due to the interaction between SNX1 and SNX6^{16,17}. Consistent with these reports, we observed a reduction of SNX1-GFP in *snx5/6* KO cells (Fig. S4D and E). Thus, the concomitant removal of SNX5 and SNX6 also severely affected SNX1 in mammalian cells. As a result, the Rab11 compartment was increased in *snx5/6* KO cells compared to control (Fig. 2C and D). This phenotype was reminiscent of the one we had

observed previously in FERARI KO cells⁷. Therefore, we asked whether SNX5 and SNX6 could interact with FERARI. FERARI members RBSN-5 and VIPAS39 specifically co-precipitated with SNX6 but not with SNX5 (Fig. 2E) indicating a link between the cargo adaptor SNX6 and the tether FERARI. This interaction is likely to be direct through interaction with RBSN-5 as in *C. elegans* (Fig. 2F). Taken together our data suggest a link between FERARI and at least SNX6. In addition to the connection with FERARI, SNX5 and SNX6 have probably additional roles. In fact, knock-down and knock-out of SNX5/6 in RPE cells was reported to yield a defect in CI-MPR retrograde transport to the TGN^{16,17}. We reproduced this phenotype in *snx5/6* KO HeLa cells (Fig. 2G). This role in retrograde transport is independent of the one that involves FERARI, as FERARI KO cells did not impede CI-MPR retrograde transport to the TGN (Fig. 2H). Nevertheless, our results are consistent with a role of at least SNX6 in FERARI and Rab11-dependent recycling to the plasma membrane. This role is expected to be conserved from *C. elegans* to mammalian cells. The difference in phenotypes is most likely related to differences in SNX1 stability, which is not affected in *C. elegans* and where we still observe SNX-1 tubules. The variation between the systems is most likely due to the greater specialization in mammals. The worm contains only one member of the SNX5/6 pair, SNX-6, and similarly the SNX1/SNX4 pair is only represented by SNX-1. Therefore, it is conceivable that SNX-1 might be less dependent on SNX-6 binding for stability. Taken together, our data so far suggest that cargo flow and cargo adaptors may contribute to the regulation of the length of the kiss.

RAB-5-positive structures contact the SNX-1 compartment via kiss-and-run

If cargo flow and cargo adaptors are regulating the length of the RAB-11 kiss, then cargo influx into the SNX-1 compartment might likewise be regulated. Incoming cargo from the plasma membrane is transported in RAB-5 endosomes. Therefore, we explored how Rab5 endosomes would interact with the SNX-1 sorting compartment. Similar to what we had observed for RAB-11 vesicles, RAB-5 vesicles contacted the SNX-1 structures by kiss-and-run (Fig. 3A). Moreover, even the periodicity of 7 sec was the same than the one observed for RAB-11 vesicles previously (Fig. 3 compare B and C). Therefore, we tested next, whether FERARI would be involved in tethering RAB-5 and SNX-1 structures. Knocking down FERARI members reduced the residence time of RAB-5 endocytic vesicles on SNX-1 structures (Fig. 3A and B), indicating that FERARI is indeed responsible for RAB-5 dependent kiss-and-run of endocytic vesicles on sorting structures. FERARI-mediated kiss-and-run of Rab5 vesicles with SNX1 sorting compartments is conserved in mammalian cells (Fig. 3D and E). Moreover, the periodicity was 4 sec, the same as we observed for the Rab11 kisses (compare Fig. 1H and Fig. 3E). Our results are consistent the notion of FERARI-mediated cargo influx into the sorting compartment via RAB-5 endocytic vesicles.

Early endosomes can undergo kiss-and-run with sorting compartments

We next asked whether the RAB-5 compartments that undergo kiss-and-run might be early endosomes. One of the hallmarks of early endosomes is that they can fuse with each other^{18,19}. Thus, we analyzed our data for events in which RAB-5 entities would undergo homotypic fusion and then contact SNX-1 positive structures in a kiss-and-run event. Indeed, we observed RAB-5 compartments fusing with each other and then go on to contact SNX-1 compartments and then move away to fuse with another early endosome (Fig. 4A, movie 5). Therefore, we assume that at least a subset of the RAB-5 compartments that undergo kiss-and-run with sorting compartments are early endosomes. We speculate that during the kiss cargo will be exchanged between the early and the sorting compartment.

SNX-6 is required for efficient kiss-and-run of Rab5-positive endosomes

Therefore, we asked next whether the cargo adaptor SNX-6 would not only regulate cargo efflux but also cargo influx. Upon knock-down of SNX-6, we observed an increase of the co-localization of RAB-5 with SNX-1 (Fig. 4B), which might be an indication for an increase in the residence time of RAB-5 vesicles on sorting endosomes. Indeed, when we measured the residence time of RAB-5 positive vesicles on SNX-1 endosomes, we observed a large increase, similar to what we noticed for RAB-11 (Fig. 4C compare to Fig. 1D). In contrast to the effect on RAB-11 vesicles, which were smaller in *snx-6(RNAi)* animals, RAB-5 vesicles were generally larger under the same condition (Fig. 4D, compare to Fig. 1F). Similarly, we observed an increased co-localization of Rab5 and SNX1 as well as an increase in the size of the co-localizing structures in *snx5/6* KO cells (Fig. 4E and Fig. S4F). Our data suggest that SNX-6 traps incoming cargo from the RAB-5 compartment and thereby provide vectorial transport into the sorting compartment, while the ordered release of cargo by SNX-6 into RAB-11 vesicles regulates efflux from the sorting compartment.

Kiss-and-run at SNX-1 sorting compartments might be a common feature

Given our data above, we were wondering, whether this mechanism of kiss-and-run on endosomal membranes is even more widespread and asked whether other RAB GTPases could interact with FERARI. To this end, we performed a yeast-two-hybrid assay with RAB-10, the other RAB GTPase known to act on endosomes in *C. elegans* (Fig. S4B). RAB-10 is involved in recycling to the basal-lateral membrane in polarized cells (C. C.-H. Chen et al. 2006). RAB-10 interacted specifically with the FERARI member Rabenosyn 5. Notably, RAB-7 did not interact with any FERARI member in this assay, suggesting that RAB-7 positive structures would not undergo FERARI-mediated kiss-and-run. Indeed, we never observed any kiss-and-run of RAB-7 vesicles with the SNX-1 compartment. Larger RAB-7 compartments were stably connected to SNX-1 and did not move around like the smaller vesicles (Fig. S5A and Suppl. Movie 1). In contrast, homotypic fusion events were frequently observed (Fig. S5B and Suppl. Movie 1). Similarly, we failed to observe kiss-and-run between Rab7 and SNX1 in mammalian cells (Fig. S5C).

To further explore the possible connection of RAB-10 and FERARI-mediated kiss-and-run at sorting compartments, we determined the localization of RAB-10 in comparison to SNX-1. We observed RAB-10 vesicular structures docked onto the SNX-1 compartment (Fig. 5A, movie 7), similar to what we had observed for RAB-11 previously⁷ and for RAB-5 (Fig. 3D). Next, we explored the effect of loss of RAB-10 on SNX-1 (Fig. 5B). Worms carrying the *rab-10* loss-of-function allele (*ok1494*) showed accumulations of enlarged SNX-1 compartments that were drastically enlarged by *vps-45* and *spe-39(RNAi)*. This phenotype was not observed in *rab-10(ok1494); vps-33.2(RNAi)* worms, implying that the effect was not due to a lack of CHEVI. CHEVI is a potential tethering complex consisting of at least SPE-39 and VPS-33.2². Similarly, in mammalian cells, Rab10 knockout resulted in enlarged SNX1 structures (Fig. 5D). Moreover, RAB-10 vesicles undergo kiss-and-run similar to RAB-5 and RAB-11, and this kiss-and-run is dependent on FERARI in *C. elegans* (Fig. 5E-G, movie 8) and mammalian cells (Fig. 5H, movie 9). Finally, the co-localization between the FERARI subunit RME-1 and RAB-10 is strongly increased in *snx-6(RNAi)* animals (Fig. 5I). Therefore, different endocytic vesicles can interact with the sorting compartment in a FERARI-dependent manner presumably in order to exchange cargo. We surmise that RAB-5 vesicles provides cargo that is transferred via the sorting compartment into RAB-10 and RAB-11 recycling entities.

FERARI interacts with distinct sets of SNAREs for RAB-11 and RAB-10 mediated recycling

RAB-11 is chiefly responsible for recycling to the apical membrane, while RAB-10 promotes recycling to the basal-lateral membrane^{20,21}. The fusion of the RAB-11 and RAB-10 vesicles with the sorting compartment is mediated by SNAREs. We were wondering whether the same or a different set of SNAREs would be involved in the fusion event. We have shown previously that the syntaxins SYX-6 and SYX-7 are involved in the fusion of RAB-11 vesicles with the SNX-1 compartment⁷. RAB-10 appears to use a largely non-overlapping set of SNAREs. The three different SNAREs *syx-16*, *vamp-7* and *vti-1* indeed showed elongated RAB-10 tubules characteristic of FERARI knock-downs, but had no effect on RAB-11 compartments (Fig. 6A and B)⁷. In contrast, knockdown of the two SNAREs *syx-6*. However, knockdown of the sorting endosomal SNARE SYX-3 affected both RAB-10 and RAB-11 endosomes (Fig. 6A and C). Moreover, SYX-3 partially co-localized with SNX-1 tubular networks, RAB-10 and the FERARI member RME-1 (Fig. 6D and E, movie 10). Collectively our data suggest that FERARI uses a common t-SNARE and a selective set of v-SNAREs to mediate fusion of RAB-10 vesicles with the SNX-1 compartment.

Regulated cargo flux from RAB-5 endocytic vesicles into RAB-11 recycling vesicles requires additional adaptors.

Since the SNX-1 sorting compartment has at least two outlets, RAB-10 and RAB-11 vesicles, it is reasonable to assume that SNX-6 is not the only factor regulating cargo flux. Indeed, different other cargo adaptors were postulated to play roles in cargo sorting during endosomal recycling. For example, the ESCRT machinery sorts cargo into the degradative pathway away from recycling cargo^{3,22}. Specific

sorting nexins (SNX17 and SNX27) as well as AP1 have been described to promote recycling of cargo²³,²⁴. Therefore, we decided to analyze the effects of these cargo adaptors on cargo flow from RAB-5 endocytic vesicles into RAB-11 recycling structures via the SNX-1 sorting endosome (Fig. 7A; model). First, we turned to HGRS-1, the *C. elegans* homolog of mammalian Hrs, a subunit of ESCRT-0 necessary for shunting cargoes into the degradative pathway. HGRS-1 should not interact with recycling cargo and would therefore not interfere with its efflux into the sorting compartment. GFP-HGRS-1 was frequently found on RAB-5 compartments (Fig. 7B, movie 11). In addition, RFP-RAB-5 vesicles also often contained a domain with HGRS-1 (Fig. 7C, movie 12), consistent with the notion that they are early endosomes (Fig. 4A). These results support our model that ESCRT-0 might sequester cargo away for the degradative pathway, while the remaining cargo would be free to diffuse into the SNX-1 sorting compartment during the kiss of RAB-5 early endosomes with SNX-1 compartments (Fig. 3A and B). The directionality of the flow would be brought about by cargo binding by SNX-6. Analogously, we assumed that vectorial flow into recycling vesicles would depend on cargo adaptors in the RAB-11 compartment. To test this hypothesis, we considered the more specialized cargo adaptors SNX-17 and SNX-27 and the adaptor complex AP1 for clathrin-dependent delivery of cargoes to the plasma membrane²³. When we knocked down these cargo adaptors, we observed an increase in the size of the SNX-1 sorting compartment, consistent with an accumulation of cargo in these structures (Fig. 7D, black arrows, Fig. S5D-F). In addition, knockdown of SNX-17 or two subunits of AP-1 led to accumulation of hTfR in enlarged SNX-1 positive compartments (Fig. 7D white arrows and E). Moreover, we observed structures that were filled with SNX-1, which also often contained hTfR (Fig. 7D, white arrowheads and asterisks). *snx-27(RNAi)* did not lead to hTfR accumulations, indicating that it may not be involved in hTfR recycling to the plasma membrane. However, since we observed the enlargement of the SNX-1 sorting compartment, we tested whether other cargoes were trapped under these conditions. Indeed, we found that Glut1 was trapped in SNX-1 compartments, when SNX-27 was missing (Fig. S5E), consistent with data from mammalian cells^{25,26}. Taken together, our data support the hypothesis of cargo influx from RAB-5 vesicles into SNX-1 sorting endosomes, where the vectorial transport is ensured by SNX-6, while the retention of cargo into RAB-11 structures would be mediated by adaptor complexes such as AP1 or SNX-17; both processes would be coordinated by FERARI.

Discussion

In this study, we revealed three key aspects in endocytic recycling. First, we showed that the recycling system is easily adaptable to changes in cargo loads it needs to process, and that the cargo concentration is a key determinant in the length of the kiss between recycling and sorting endosomes. Second, we provide strong evidence that the cargo flux and sorting in the endosomal system is dependent on cargo-cargo adaptor interactions and that the availability of these adaptors and probably their binding affinities regulate sorting into different pathway. Third, our data support the notion that the FERARI tethering platform coordinates recycling by its ability to facilitate kiss-and-run of Rab5 early endosomes and Rab10 and Rab11 recycling endosomes with the sorting compartment.

We envisage a model in which Rab5 endocytic vesicles/early endosomes on their way from the plasma membrane inwards kiss SNX1 sorting endosomes. During this kiss, cargo destined for immediate recycling could already exit the Rab5 compartment. We predict negative selection in this process in that ubiquitinated cargo, which interacts with the ESCRT-0 component Hrs would have to remain in the Rab5 compartment, while un- or deubiquitinated cargo would be free to leave. Attraction by the negative membrane curvature during the kiss facilitate the movement of membrane proteins and specific lipids towards the sorting endosome^{12,13}. The length of the kiss would depend on the amount of cargo diffusing into the sorting compartment (further discussion below). Backflow of cargo would be prevented by its binding to the cargo adaptor SNX6 and potentially other cargo adaptors in the sorting compartment. In fact, we found that loss of function of SNX-17 and SNX-27 resulted in enlarged SNX-1 compartments and cargo accumulation. SNX17 and SNX27 were shown to be involved in recycling through retriever and retromer recycling pathways^{23,24}. Combinatorial low affinity interactions of cargo with different adaptors may drive sorting in the SNX1 sorting compartment²⁷. The efflux of cargo would occur into RAB-10 or RAB-11 vesicles, that would kiss in a similar way than RAB-5 endosomes. In the case of RAB-11, we surmise that AP1 is critical to retain the cargo in the RAB-11 compartment and avoid backflow into the sorting compartment. The presence of AP1 on tubular recycling endosomes has been shown previously⁴. The retention could be helped by either the concentration of AP1 or to a higher affinity of the cargo for AP1 than for a SNX cargo adaptor.

Cargo binding affinities to different adaptors have been determined and support our model. SNX5 and SNX6 binding constants to the sorting motif of Cl-MPR were measured to be $K_D = 18 \mu\text{M}$ and $36 \mu\text{M}$ ²⁸. The *Chlamydia* toxin IncE that blocks retromer by binding to SNX5 and SNX6 showed a binding constant of $K_D = 0.5\text{-}1 \mu\text{M}$, indicating that this higher affinity would be sufficient to outcompete other cargoes. For SNX17, a high binding affinity to P-selectin was reported ($K_D = 2.7 \mu\text{M}$)²⁹. SNX27 bound a motif of LRFN2 with a $K_D = 1.6 \mu\text{M}$ ³⁰ and together with VPS26 the binding affinity to a Kir3.3 sequence was $K_D = 0.84 \mu\text{M}$ ²⁶. These dissociation constants would allow a flow of cargo from SNX5 and SNX6 to SNX17 and SNX27. AP1 was reported to bind to an MPR46 tail with a $K_D = 11\text{-}15 \text{ nM}$ ³¹, while AP2 $\mu 2$ subunit bound a TGN38 cytosolic domain with a $K_D = 58 \text{ nM}$ ³² and AP4 $\mu 4$ bound to a selected peptide with an affinity of $K_D = 7 \mu\text{M}$ ³³. These results show higher affinities of AP adaptor complexes for cargo than SNX5 and SNX6, again allowing a possible flow of cargo from SNX1 compartments into vesicles containing AP1. Therefore, our data are consistent with the notion that the directionality of cargo flow in the endocytic system is regulated by an increase of binding affinities between the cargoes and their interaction partners during the sorting process.

Since the binding affinities during the sorting process are relatively low, mis-sorting is prone to happen. Kiss-and-run of Rab5 endosomes on their journey inward and of Rab11 and Rab10 endosomes outward provide opportunities to correct mistakes in sorting and may increase fidelity of the entire process. Moreover, sorting is not perfect in that there is always some bulk flow. This phenomenon is probably best recognized in at the endoplasmic reticulum, where ER-resident proteins escape routinely in COPII vesicles

to the Golgi. The cell has even evolved retrieval system to counteract this loss of ER proteins from the ER³⁴⁻³⁶. Thus, kiss-and-run would make the endocytic system more robust and less error-prone.

We show that the length of the kiss of the RAB-11 endosomes depends on cargo availability in the sorting endosome. We assume that the 'measure' of the cargo concentration would be the inability to close the neck and pinch off vesicles caused by obstructing cargo present in the neck. Since the cargo size is quite bulky in comparison with the pore size⁸⁻¹⁰ and the building of a spiral or ring structure by RME-1 is essential for pinching, the presence of cargo molecules might cause an interruption of the process until cargo sorting is completed.

Our proposed sorting model explains the observed kiss-and-run of vesicles in the endosomal system. It also provides a simple and efficient mechanism that allows for cargo sorting mistakes and step-by-step enrichment of specific cargo into different cargo carriers. The simplicity of regulating the length of cargo exchange through the presence of cargo itself would provide a way to deal with higher and lower cargo loads during cell development, changing nutrition conditions and stress.

Material And Methods

Worm husbandry

C. elegans worms were grown and crossed according to standard methods³⁷. RNAi was performed as previously described³⁸. All experiments were carried out at 20°C, and worms were imaged at the young adult stage (with only few eggs).

The following worm strains and transgenes were used in this study: *pwls206[vha6p::GFP::rab-10 + Cb unc-119(+)]*, *pwls782[Pvha-6::mCherry::SNX-1]*, *pwls414[Pvha-6::RFP::rab-10, Cb unc-119(+)]*, *dkls218[Popt-2-GFP-syx-3; Cb unc-119(+)]*, *pwls621[vha-6::mCherry-RME-1]*, *pwls72[vha6p::GFP::rab-5 + unc-119(+)]*, *pwls170[vha6p::GFP::rab-7 + Cb unc-119(+)]*, *pwls90[Pvha-6::hTfR-GFP; Cbr-unc-119(+)]*, *qxEx2247 [Pvha-6::Glut1::GFP]*, *pwls69[vha6p::GFP::rab-11 + unc-119(+)]*, *pwls87[Pvha-6::GFP::rme-1; Cbr-unc-119(+)]*, *[Pdhs-3::dhs-3::GFP]*, *pwls481[Pvha-6::mans-GFP, Cbr-unc-119(+)]*, *pwls518[vha-6::GFP-HGRS-1]*, *pwls846[Pvha-6-RFP-rab-5; Cb unc-119(+)]*, *rab-10(ok1494)*.

Microscopy of *C. elegans*

Live microscopy on worms was performed as described^{7,38}. In short, worms were immobilized on 2% agarose pads on microscopy slides using levamisole (50 mM); cover slips were sealed using Vaseline. Overview images were acquired with an Olympus Fluoview FV3000 system using a high sensitivity spectral detector (HSD) at a standard voltage setting (PTM) of 500. For higher resolution, the Galvano scan device was applied. A 60x objective with silicone oil was used, resulting in a pixel size of 0.098 µm. Laser intensities were at 4–10% for both 488 (GFP) and 561 (RFP, mCherry) wavelengths. Sampling

speed was 8.0 $\mu\text{s}/\text{pixel}$ with a zoom factor of 2.1. All images for corresponding experiments were processed with the same settings to insure comparable results.

High resolution 3D images and movies were obtained with a Zeiss LSM 880 microscope with Airyscan capabilities. Fast mode in the Zen Black software was used for all images. The higher than usual levamisole concentration of 50 mM was used to insure very little movement during image acquisition. For movies, resolution was traded in for speed by reducing the averaging to 2-4x, resulting in the required frame speeds of 0.5–1.0 seconds to follow vesicles. To catch high enough numbers of vesicles a region of approximately 70 μm^2 was covered (about 2 intestinal cells). Movement could be observed up to 30–45 min after immobilization of worms. From these overview movies, smaller regions of 70 x 70 pixels were selected, showing only 1–2 vesicles and events. These movies were then quantified. We observed persistent movement in many cells, and events were mainly limited by the use of only one imaging plane (due to speed limitation of the microscope). The “StackReg” plugin in Fiji was used to get rid of worm shaking and drifting motions. “Bleach correction” was used to avoid irritating blinking during repeated viewing of movies (overall, bleaching was minimal).

Compartment quantifications

RAB-10 tubule length was measured with the freehand line ROI function in Fiji. Since only one z-plane was used, this leads to an underestimation of the true length of tubules, but since FERARI phenotypes were exceptionally strong, no further measurements were deemed necessary. Mander’s Coefficients for co-localization between compartments were measured with the JACoP plugin of Fiji, using all available z-planes over whole intestinal cells for 10 worms each.

GFP-Knock-in at the Rab11 locus in HeLa cells

GFP construct was inserted into the N-terminal of Rab11 at the endogenous level by using CRISPR/Cas9 homology directed repair. The following strategy was taken to insert GFP into Rab11 genome (Fig. S6). Two guide RNAs were designed from introns before and after first exon of Rab11. Annealed oligonucleotides were cloned into two different plasmids, Px458 mCherry (kindly provided by Mirjam Pennauer), and Px459 Puro (addgene) plasmids, respectively. Template DNA was prepared PCR method. As indicated in the scheme 5 PCR product was synthesized. GFP was synthesized by using a GFP containing plasmid as a template and for the rest, genomic DNA from HeLa cells served as template. All these PCR products was cloned into pUC19 plasmid (Addgene; 50005, kindly gifted by Dr. Shahidul Alam, Pharmazentrum) by Gibson assembly method. After transformation, sequencing was done confirm the insertion template into the vector. 2 gRNAs containing vectors and the template containing vector were then transfected into HeLa cells by using Helix-in (OZ biosciences) transfecting reagent based on the manufacturers protocol. After 7 days of transfection cells were FACS sorted and GFP⁺ cells were collected. For the confirmation of the GFP-knock-in, PCR and western blot was performed.

Cell culture, transfection and CRISPR–Cas9 KO in mammalian cells

HEK293 and HeLa cells were cultured and maintained in DMEM (Sigma) high-glucose medium with 10% FCS (Bioconcept), penicillin–streptomycin (1%), sodium pyruvate and l-glutamine. Cells were plated 1 d before transfection at 60–70% confluency and later transfected for 48 h using Helix-in (OZ biosciences) transfection reagent according to the manufacturer's instructions. A 1–2 µg of DNA was used per reaction based on a 10-cm dish. For CRISPR–Cas9-mediated KO, guide RNAs were selected using the CRISPR design tools (<http://chopchop.cbu.uib.no/> and <https://www.benchling.com/>). A list of oligonucleotides is provided in Table S1. Two guide RNAs were designed from two different exons for each target gene. Annealed oligonucleotides were cloned into two different plasmids, Px458 GFP and Px459 Puro, respectively. In brief, HeLa cells were seeded at 2×10^6 cells per 10-cm dish. The following day, cells were transfected with 2.5 µg of the plasmids (control vectors without insert or vectors containing a guide RNA against the target gene). Transfecting medium was exchanged with fresh medium after 4 h. Cells were treated with puromycin for 24 h after transfection followed by FACS sorting (for GFP + cells) the next day. For FACS sorting after 48 h of transfection, cells were trypsinized and resuspended in cell-sorting medium (2% FCS and 2.5 mM EDTA in PBS) and sorted on a BD FACS AriaIII Cell Sorter. GFP-positive cells were collected and seeded in a new well.

Immunoprecipitation assays

HEK293 cells were co-transfected with the indicated DNA constructs. After 36–48 h of transfection, protein extracts were prepared in lysis buffer (50 mM Tris/HCl pH 7.5, 150 mM NaCl, 1% NP-40) and Halt protease inhibitor cocktail (Thermo Scientific; 186 1279) at 4°C for 20 min followed by centrifugation at 4°C for 20 min at 13,000 r.p.m. Immunoprecipitations were performed as previously described⁵⁵. In brief, protein extracts were incubated with Trap beads (nanobodies for GFP (GFP-Trap_A; gta-20-chromotek), for 6 h at 4°C with rotation, and then washed five times with lysis buffer (1 ml). Protein complexes were eluted by heating beads for 5 min at 95°C in 2× sample buffer and resolved by SDS–PAGE on 10% and 12.5% gels followed by immunoblot analysis. Blots were developed using Amersham ECL Prime Western Blotting Detection Reagent (RPN2236) and X-ray film (Amersham Hyperfilm ECL-28906839).

Western blot analysis

Cells were collected and lysed in lysis buffer (50 mM Tris/HCl pH 7.5, 150 mM NaCl, 1% NP-40) containing a protease inhibitor cocktail (Roche). Protein concentrations were determined in all experiments using the Bio-RAD protein assay (Bio-RAD, 500-0006) and 20–40 µg of total protein was loaded onto SDS–PAGE gels ranging between 10 and 15% acrylamid before transfer onto nitrocellulose membranes (Amersham Protran; 10600003). Membranes were blocked with 5% milk, 0.1% Tween20 for 60 min at room temperature. The primary antibody incubation was overnight at 4°C and the secondary HRP-coupled antibodies were incubated for 1 h at room temperature. For RAB10, SNX5 and SNX6 detection, primary antibodies were diluted in Can Get Signal™ solution 1 overnight. The secondary HRP-coupled antibodies were diluted in Can Get Signal™ solution 2 for one hour. The blots were developed using western Blotting detection kit WesternBright™ ECL (advansta; K-12045-D50) and the Fusion FX7 (Vilber Lourmat) image acquisition system.

Immunostaining in mammalian cells

Cells were plated onto sterile 13-mm glass coverslips. Cells were fixed with 2% paraformaldehyde for 15 min, permeabilized (0.1% Triton X-100 in PBS) for 5 min and blocked with 2% BSA containing 5% goat serum in PBS for 1 h. Coverslips were incubated in primary antibodies for 2 h and washed five times in PBS followed by a 1-h incubation with fluorescently tagged secondary antibodies. After secondary antibody incubation, coverslips were washed further five times in PBS and mounted onto glass slides using Fluoromount-G (Southernbiotech; 0100-01). Images were taken with an inverted Olympus FV3000 confocal microscope (Olympus, Wallisellen, Switzerland) using a Plan Apochromat N 60x/1.40 silicon oil objective or an Axio Observer Zeiss microscope (Zeiss, Oberkochen, Germany) with z stacks. Co-localization studies were performed using the ImageJ co-localization plugin JACoP.

CI-MPR uptake and trafficking analysis

Cells were incubated with 10 µg/ml mouse anti-CI-MPR monoclonal antibody (ThermoFisher MA1-006) in serum-free DMEM for 1 h, rinsed with PBS, fixed with 4% paraformaldehyde, solubilized with Triton-X and immunostained with 1:500 anti-Giantin (rabbit) antibody (BioLegend cat 924302) and then fluorescent anti-rabbit and anti-mouse antibodies 1:500.

Live cell imaging in mammalian cells

For live imaging, cells were plated in an 4-well chambered coverglass (Ibidi µ-slide; Ibidi GmbH, Germany) and medium was replaced with warm imaging buffer (5 mM dextrose (D(+)-glucose, H₂O, 1 mM CaCl₂, 2.7 mM KCl, 0.5 mM MgCl₂ in PBS) just before imaging. Images were taken at 37°C on an inverted Axio Observer Zeiss microscope using a Plan Apochromat N 63x/1.40 oil DIC M27 objective with a Photometrics Prime 95B camera. Z-stack images were processed using the OMERO client server web tool and Fiji. For kiss-and-run studies, live movies were taken at 37°C by using imaging buffer on a DeltaVision OMX Optical Microscope equipped with CO₂ supply. 60x/1.524 oil objective was used for image acquisition. According to the Meta data, the frame rate was 750–780 milliseconds.

Quantification of Rab11-positive endosomes

Segmentation and analysis were performed on manually chosen ROIs using a custom script for Fiji57 as follows. First, a 3D white top-hat filter58 was applied to the original image to homogenize the background and used to compute 3D seeds59 with subpixel accuracy. Next, objects were segmented on the original image using an iterative threshold60 and converted to labels. Touching objects were then separated by a 3D watershed61 using the previously identified seeds on the label image. The resulting image was then added to the 3D ROI Manager10 to exclude remaining laterally touching objects and finally perform intensity and size measurements per object. A total of 2,500-3,000 Rab11-positive particles were analyzed from 40–50 cells for each condition. The script is available upon request.

Antibodies

The following antibodies were used in this study: polyclonal. Polyclonal rabbit anti-GFP (TP401; Torrey Pines; 1:2,000 for western blotting and 1:200 for immunostaining), Rab10 (D36C4) Rabbit mAb (#8127, Cell signaling, 1:1000 for western blotting), Rab11 Anti-Rab11 antibody (ab3612, abcam, 1:1000 for

western blotting), Recombinant Anti-SNX5 antibody (ab180520, abcam, 1:1000 for western blotting). Purified Mouse Anti-SNX1 (611482, BD biosciences, 1:100 for IF), SNX6 mouse monoclonal antibody (D-5) (sc-365965, Santa Cruz, 1:1000 for western blotting), For pulldowns, Trap beads (nanobodies) were used. GFP-Trap_A (chromotek, gta-20) was used for GFP pulldowns. HRP-conjugated goat anti-mouse IgG (H + L) secondary antibody (Thermo Fisher Scientific; 31430; 1:10,000) and polyclonal HRP-conjugated goat-anti-rabbit IgG (Thermo Fisher Scientific; 31460; 1:10,000) were used (incubated for 1 h at room temperature) to detect bound antibodies with Blotting detection kit WesternBright™ ECL (advanta; K-12045-D50). Alexa Fluor 488–goat anti-rabbit IgG (H + L) (Invitrogen; A-11034) and Alexa Fluor 594–goat anti-mouse IgG (H + L) cross-adsorbed secondary antibodies (Invitrogen; R37121) were used for immunofluorescence.

DNA and Plasmid sources

The following commercially available plasmids were obtained: GFP-VIPAS39 (Sino.Bio; HG22032_ACG), GFP-Rabenosyn-5 (Addgene; 37538), turbo-GFP-SNX1 (Origene; RG201844), GFP-RAB11 (Addgene; 12674). The plasmids Px458 GFP (Addgene; 48138) and Px459 Puro (Addgene; 62988) were used for cloning gRNAs. mCherry-SNX1 was created by PCR amplifying mCherry from mCherry-Rab11 construct (Plasmid #55124) and ligating into NotI/PmeI sites of SNX1 vector (Origene; RG201844). Turbo-GFP was deleted from the plasmid by restriction digestion (NotI/PmeI). PCR synthesized mCherry was ligated into the linearized SNX1 vector by using the Roche rapid ligation kit. mCherry was cloned into EGFP-RAB10 vector (Addgene; 49472) after deleting EGFP. mCherry was synthesized from mCherry Rab11 plasmid (Addgene: 55124).

Declarations

Acknowledgements

We thank Mirjam Pennauer (Biozentrum) and Shahidul Alam (Pharmazentrum) for sharing the Px458 mCherry plasmid and the pUC19 plasmid, respectively. The Imaging Core Facility of the Biozentrum facilitated the generation of movies and image analysis, in particular Alexia Loynton-Ferrand and Laurent Guerard. Cells were sorted in the FACS Core Facility of the Biozentrum. We are grateful to Jean Gruenberg for critical comments on the manuscript. Barth Grant and Pingsheng Liu are acknowledged for sharing strains. Some strains were provided by the CGC, which is funded by the NIH Office for Research Infrastructure Programs (P40 OG010440). This work was supported by the Swiss National Science Foundation (CRSII3_141956, 31003A_141207, 310030_197779 to A.S) and the University of Basel.

References

1. Scott, C.C., Vacca, F. & Gruenberg, J. Endosome maturation, transport and functions. *Semin Cell Dev Biol* **31**, 2–10 (2014).
2. Spang, A. Membrane Tethering Complexes in the Endosomal System. *Front Cell Dev Biol* **4**, 35 (2016).

3. Cullen, P.J. & Steinberg, F. To degrade or not to degrade: mechanisms and significance of endocytic recycling. *Nat Rev Mol Cell Biol* **19**, 679–696 (2018).
4. Klumperman, J. & Raposo, G. The complex ultrastructure of the endolysosomal system. *Cold Spring Harb Perspect Biol* **6**, a016857 (2014).
5. Gallon, M. & Cullen, P.J. Retromer and sorting nexins in endosomal sorting. *Biochem Soc Trans* **43**, 33–47 (2015).
6. Chen, K.E., Healy, M.D. & Collins, B.M. Towards a molecular understanding of endosomal trafficking by Retromer and Retriever. *Traffic* **20**, 465–478 (2019).
7. Solinger, J.A., Rashid, H.O., Prescianotto-Baschong, C. & Spang, A. FERARI is required for Rab11-dependent endocytic recycling. *Nat Cell Biol* **22**, 213–224 (2020).
8. Daumke, O. *et al.* Architectural and mechanistic insights into an EHD ATPase involved in membrane remodelling. *Nature* **449**, 923–927 (2007).
9. Pant, S. *et al.* AMPH-1/Amphiphysin/Bin1 functions with RME-1/Ehd1 in endocytic recycling. *Nat Cell Biol* **11**, 1399–1410 (2009).
10. Deo, R. *et al.* ATP-dependent membrane remodeling links EHD1 functions to endocytic recycling. *Nat Commun* **9**, 5187 (2018).
11. Lawrence, C.M. *et al.* Crystal structure of the ectodomain of human transferrin receptor. *Science* **286**, 779–782 (1999).
12. Roux, A. *et al.* Role of curvature and phase transition in lipid sorting and fission of membrane tubules. *EMBO J* **24**, 1537–1545 (2005).
13. Aimon, S. *et al.* Membrane shape modulates transmembrane protein distribution. *Dev Cell* **28**, 212–218 (2014).
14. Strutt, H. *et al.* Retromer Controls Planar Polarity Protein Levels and Asymmetric Localization at Intercellular Junctions. *Curr Biol* **29**, 484–491 e486 (2019).
15. Simonetti, B. *et al.* Molecular identification of a BAR domain-containing coat complex for endosomal recycling of transmembrane proteins. *Nat Cell Biol* **21**, 1219–1233 (2019).
16. Wassmer, T. *et al.* A loss-of-function screen reveals SNX5 and SNX6 as potential components of the mammalian retromer. *J Cell Sci* **120**, 45–54 (2007).
17. Simonetti, B., Danson, C.M., Heesom, K.J. & Cullen, P.J. Sequence-dependent cargo recognition by SNX-BARs mediates retromer-independent transport of Cl-MPR. *J Cell Biol* **216**, 3695–3712 (2017).
18. Gruenberg, J., Griffiths, G. & Howell, K.E. Characterization of the early endosome and putative endocytic carrier vesicles in vivo and with an assay of vesicle fusion in vitro. *J Cell Biol* **108**, 1301–1316 (1989).
19. Gorvel, J.P., Chavrier, P., Zerial, M. & Gruenberg, J. rab5 controls early endosome fusion in vitro. *Cell* **64**, 915–925 (1991).
20. Grant, B. & Hirsh, D. Receptor-mediated endocytosis in the *Caenorhabditis elegans* oocyte. *Mol Biol Cell* **10**, 4311–4326 (1999).

21. Chen, C.C. *et al.* RAB-10 is required for endocytic recycling in the *Caenorhabditis elegans* intestine. *Mol Biol Cell* **17**, 1286–1297 (2006).
22. Norris, A. *et al.* SNX-1 and RME-8 oppose the assembly of HGRS-1/ESCRT-0 degradative microdomains on endosomes. *Proc Natl Acad Sci U S A* **114**, E307-E316 (2017).
23. Chi, R.J., Harrison, M.S. & Burd, C.G. Biogenesis of endosome-derived transport carriers. *Cell Mol Life Sci* **72**, 3441–3455 (2015).
24. Tan, J.Z.A. & Gleeson, P.A. Cargo Sorting at the trans-Golgi Network for Shunting into Specific Transport Routes: Role of Arf Small G Proteins and Adaptor Complexes. *Cells* **8** (2019).
25. Steinberg, F. *et al.* A global analysis of SNX27-retromer assembly and cargo specificity reveals a function in glucose and metal ion transport. *Nat Cell Biol* **15**, 461–471 (2013).
26. McMillan, K.J. *et al.* Atypical parkinsonism-associated retromer mutant alters endosomal sorting of specific cargo proteins. *J Cell Biol* **214**, 389–399 (2016).
27. Gallon, M. *et al.* A unique PDZ domain and arrestin-like fold interaction reveals mechanistic details of endocytic recycling by SNX27-retromer. *Proc Natl Acad Sci U S A* **111**, E3604-3613 (2014).
28. Yong, X. *et al.* Mechanism of cargo recognition by retromer-linked SNX-BAR proteins. *PLoS Biol* **18**, e3000631 (2020).
29. Ghai, R. *et al.* Structural basis for endosomal trafficking of diverse transmembrane cargos by PX-FERM proteins. *Proc Natl Acad Sci U S A* **110**, E643-652 (2013).
30. McMillan, K.J. *et al.* Sorting nexin-27 regulates AMPA receptor trafficking through the synaptic adhesion protein LRFN2. *bioRxiv*, 2020.2004.2027.063248 (2020).
31. Honing, S., Sosa, M., Hille-Rehfeld, A. & von Figura, K. The 46-kDa mannose 6-phosphate receptor contains multiple binding sites for clathrin adaptors. *J Biol Chem* **272**, 19884–19890 (1997).
32. Stephens, D.J., Crump, C.M., Clarke, A.R. & Banting, G. Serine 331 and tyrosine 333 are both involved in the interaction between the cytosolic domain of TGN38 and the mu2 subunit of the AP2 clathrin adaptor complex. *J Biol Chem* **272**, 14104–14109 (1997).
33. Aguilar, R.C. *et al.* Signal-binding specificity of the mu4 subunit of the adaptor protein complex AP-4. *J Biol Chem* **276**, 13145–13152 (2001).
34. Gerondopoulos, A. *et al.* A signal capture and proofreading mechanism for the KDEL-receptor explains selectivity and dynamic range in ER retrieval. *Elife* **10** (2021).
35. Spang, A. Retrograde traffic from the Golgi to the endoplasmic reticulum. *Cold Spring Harb Perspect Biol* **5** (2013).
36. Spang, A. & Schekman, R. Reconstitution of retrograde transport from the Golgi to the ER in vitro. *J Cell Biol* **143**, 589–599 (1998).
37. Brenner, S. The genetics of *Caenorhabditis elegans*. *Genetics* **77**, 71–94 (1974).
38. Solinger, J.A., Poteryaev, D. & Spang, A. Application of RNAi technology and fluorescent protein markers to study membrane traffic in *C. elegans*. *Methods Mol Biol* **1174**, 329–347 (2014).

Figures

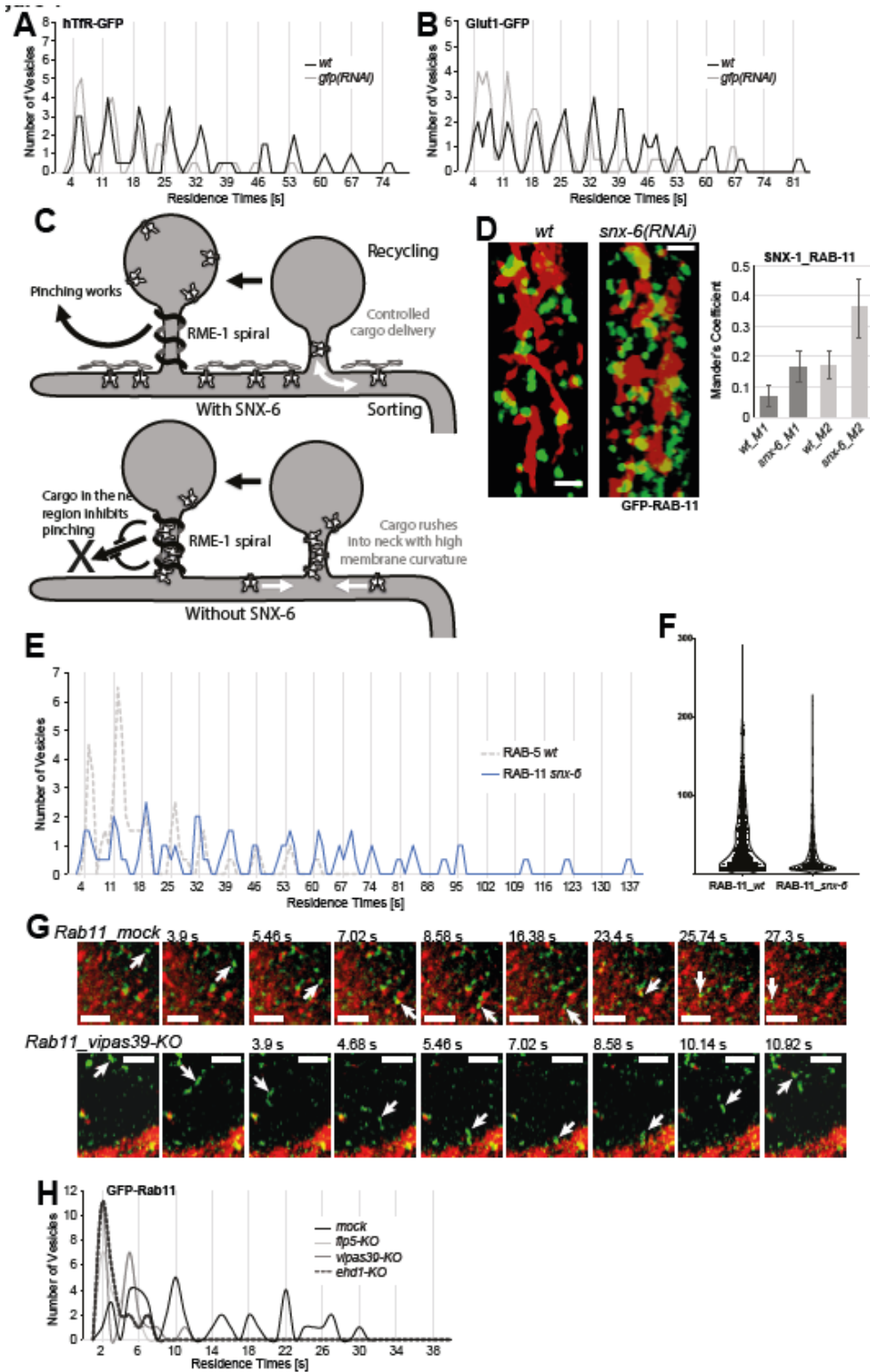


Figure 1

Cargo flow through sorting/recycling endosomes is regulated by cargo amount and cargo adaptors. (A) Residence times for hTfR-GFP vesicles decrease when cargo amount is reduced. Moving average for residence times is shown for wild-type (no knock-down, n=55) and gfp(RNAi) (n=46) (see Fig. S1F, G for

alternative graphs). Graphs with individual vesicle data are shown in Fig. S1E. (B) Residence times for Glut1-GFP vesicles decrease when cargo amount is reduced. Residence times are plotted as in (A) for wild-type (no RNAi, n=56) and gfp(RNAi) (n=54). (see Fig. S1H, I for alternative graphs). (C) Models for SNX-6 function and cargo flow through recycling endosomal networks. Schematic representation of possible role of SNX-6 as a cargo organizer in the SNX-1 compartment. Top shows regulated cargo exchange in the presence of SNX-6. Bottom shows situation without cargo adaptor SNX-6, leading to crowding in vesicle neck and blocked pinching. (D) Cargo adaptor snx-6(RNAi) leads to increased co-localization of GFP-RAB-11 vesicles with mCherry-SNX-1 networks (see Movie 1). Quantification of Mander's coefficients on the right (n=10). (E) Knock-down of snx-6 cargo adaptor causes very long residence times of kiss & run vesicles (see Fig. S3A for single vesicles). The RAB-5 wild-type vesicles from Fig. 4C are plotted as a dashed line for comparison (see also Fig. S1J). Please note the elongated x-axis to accommodate vesicles with very long residence times (n=57 for RAB-11). (F) Vesicles from snx-6 cargo adaptor knock-down worms show changes in size. RAB-11 vesicles appeared smaller (wt: n=774, snx-6: n=995) (see Fig. S3E for single worms). (G) Rab11 vesicles exhibit kiss-and-run behavior dependent on FERARI. Movie stills showing kiss-and-run of endogenously GFP-tagged Rab11 vesicles (arrow) in ctr KO and vipas39-KO HeLa cells (see also Movie 2). Scale bar: 2 μ m. (H) Rab11 vesicles dock on SNX1 networks with residence times in distinct intervals. Groups of vesicles with similar residence times appear as peaks (see also Fig. S2B for single vesicle graph, mock: n=41, vipas39-KO: n=25). This pattern is abolished in vipas39 KO cells (see Fig. S2 for ehd-1-KO and rab11fip5-KO additional data).

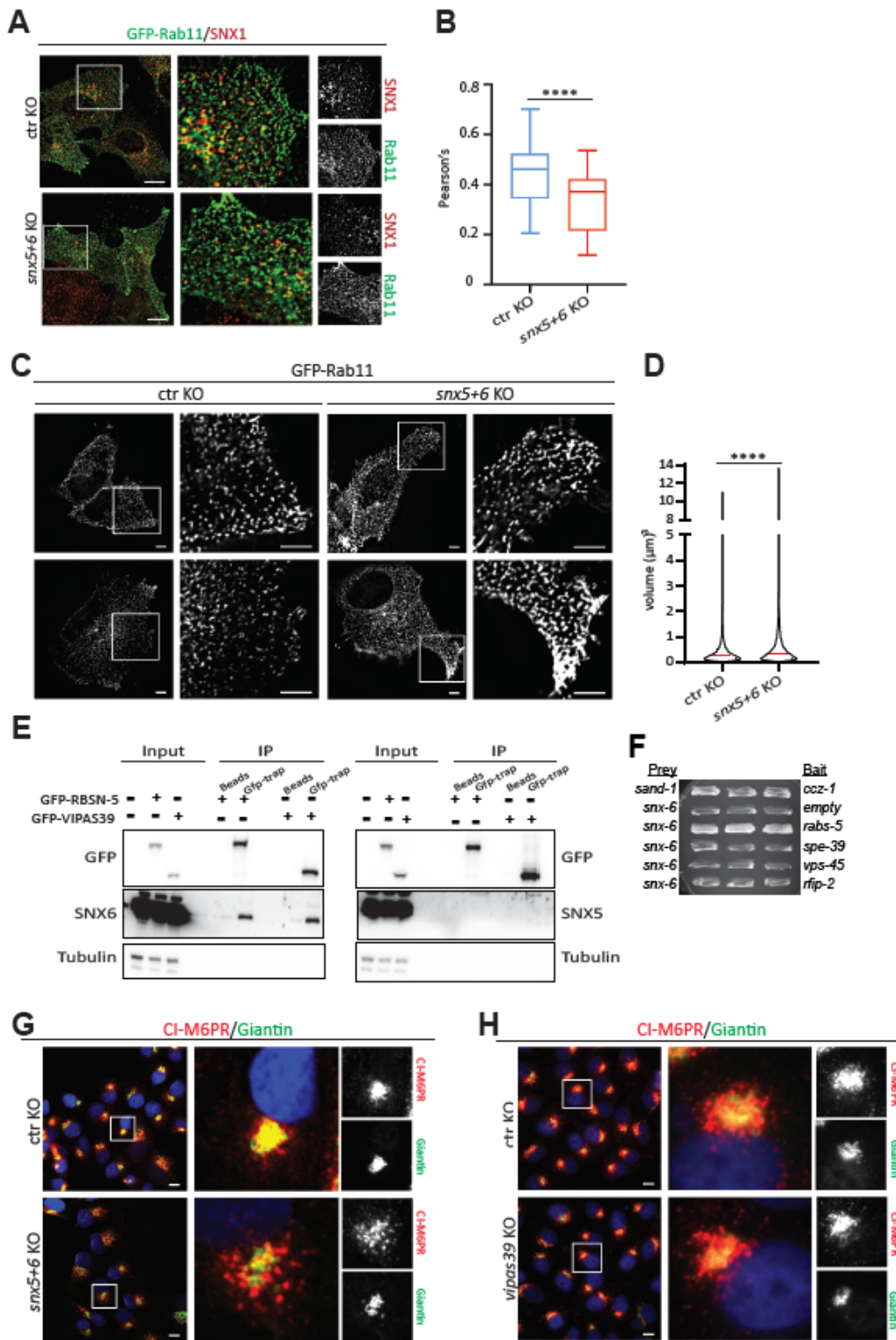


Figure 2

SNX5/6 are involved in Rab11-dependent recycling. (A) Co-localization between GFP-Rab11 and endogenous SNX1 is reduced in *snx5+6* double knock out cells. Antibodies against GFP and SNX1 were used to detect Rab11 and SNX1 by immunofluorescence, respectively. Scale bars 10 μm ; 5X magnified. (B) Quantification of the Pearson's coefficient from 65 and 71 cells from ctr KO and *snx5+6* KO cells, respectively. (C) Size of the GFP-Rab11 positive structures is increased in *snx5+6* double knock out cells

in comparison with the ctr KO cells (n= 3 independent experiments) Scale bars 10 μ m; magnification 5x. (D) Volume of the GFP-Rab11 positive particles in both CTR and KO cells were determined (volume of more than 15,000 particles were measured from each group from three independent experiments, median is shown by the red stripe). (E) Immunoprecipitation data showing that endogenous SNX6 (left panel), but not SNX5 (right panel), binds to FERARI members Rabenosyn-5 and VIPAS39 in HEK-293 cells (n= 3 independent experiments). (F) C. elegans SNX-6 interacts with RABS-5 (but not with other FERARI subunits) in Y2H assays. (G) CI-MPR trafficking is impaired in *snx5+6* KO cells. CI-MPR (red) is mostly localized in TGN (green) area in ctr KO cells and is dispersed in *snx5+6* KO cells. (H) CI-MPR localization remain unchanged in *vipas39* KO cells (n=3 independent experiments). Scale bars 10 μ m; magnification 5x.

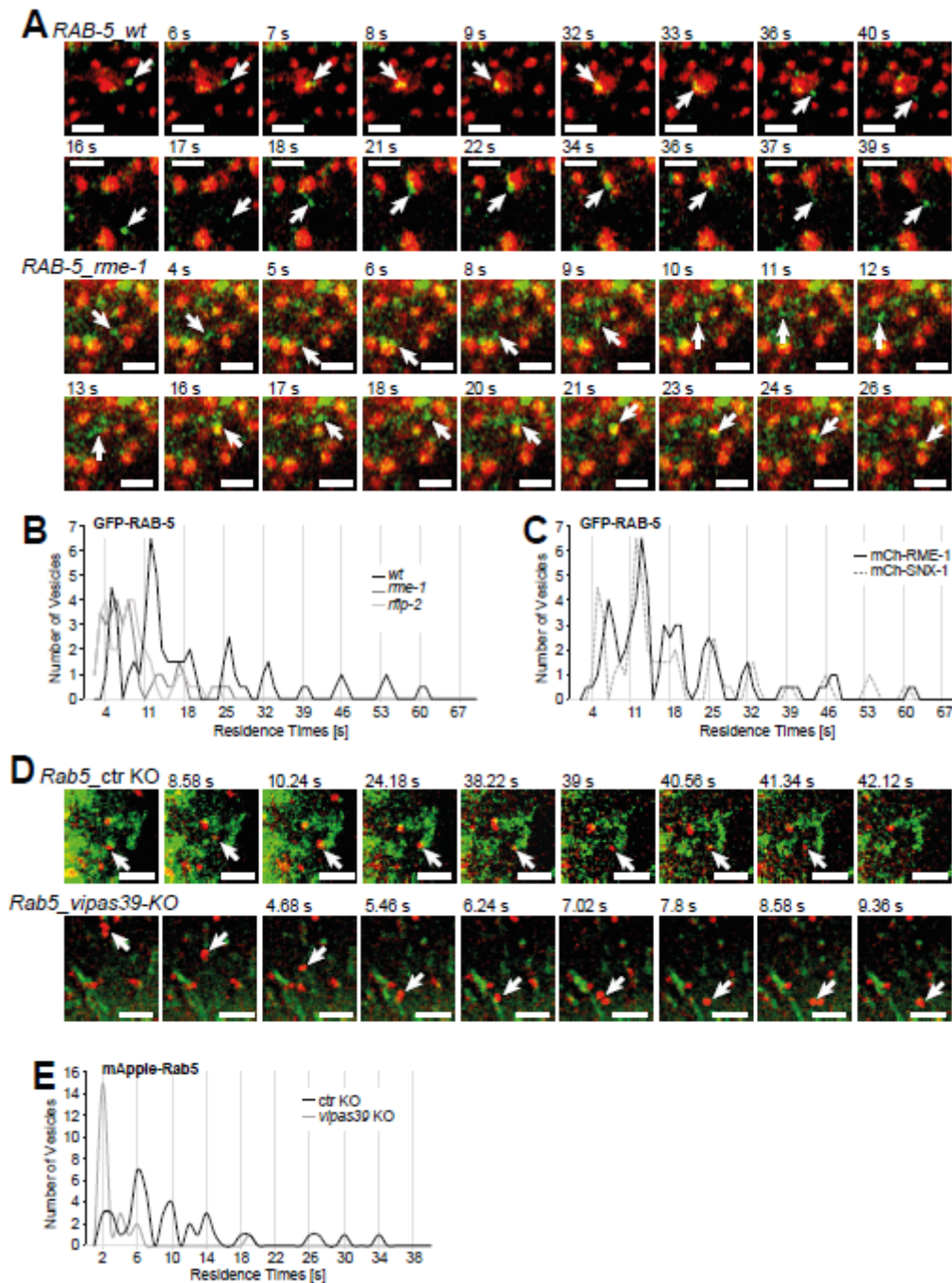


Figure 3

RAB-5 vesicles exhibit kiss-and-run behavior dependent on FERARI. (A) Movie stills showing kiss-and-run of RAB-5 vesicles (arrow) in wild-type and *rme-1*(RNAi) worms (see also Movie 3). Scale bar: 2 μ m. (B) RAB-5 vesicles dock on SNX-1 networks with residence times in distinct intervals. Groups of vesicles with similar residence times appear as peaks (see also Suppl. Fig. 2B for single vesicle graph, n=53). This pattern is abolished in *rme-1* (n=33) and *rfip-2* (n=35) knock-downs (see Fig. S3B for single vesicle plots). (C) Residence times intervals also appear in RAB-5 vesicles docking to mCherry-RME-1 compartments (wild-type from (B) as comparison, n=63) (see Fig. S3B). (D) Rab5 exhibits kiss-and-run behavior in HeLa cells stably expressing mApple-Rab5 and transiently expressing Turbo-GFP SNX1. Movie stills show representative vesicles for ctr KO and *vipas39*-KO cells (arrow) (see also Movie 4). Scale bars: 2 μ m. (E) Binning of vesicles from (D) reveals distinct intervals of residence times for Rab5 vesicles (mock: n=41, *vipas39*-KO: n=23). This pattern is abolished in *vipas39*-KO cells (see Fig. S3C for single vesicle plots).

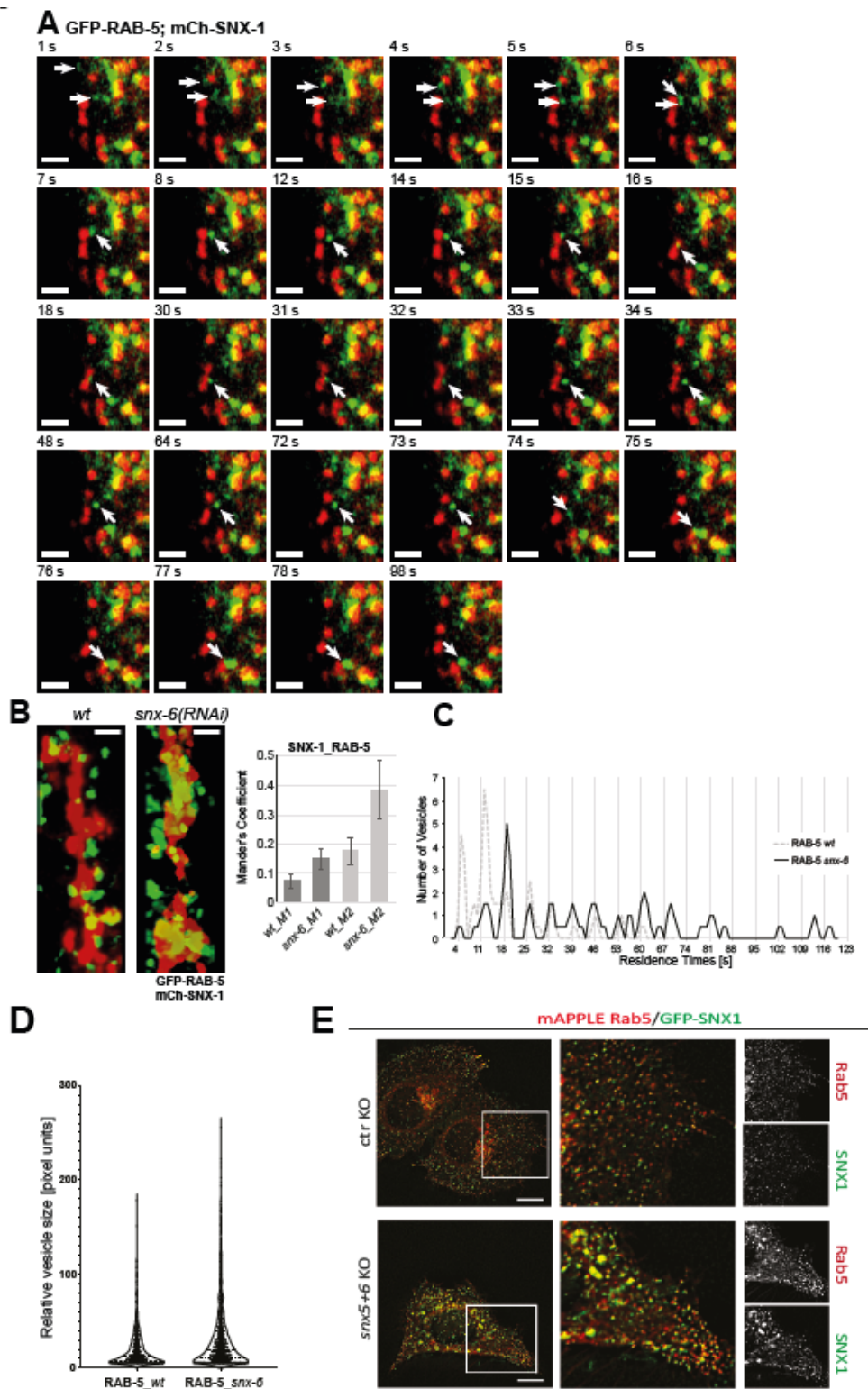


Figure 4

RAB-5 vesicles undergo homotypic fusion and kiss-and-run events on their way to the sorting endosome. (A) Movie stills for GFP-RAB-5 positive vesicles fusing, then docking on mCherry-SNX-1 compartment (kiss & run for 18 s) and finally fusing with a larger sorting endosome (with GFP-RAB-5 and mCherry-SNX-1 domains). Scale bar: 2 μ m. (B) Cargo adaptor *snx-6*(RNAi) leads to increased co-localization of GFP-RAB-5 vesicles with mCherry-SNX-1 networks (see Movie 6). Quantification of Mander's coefficients on

the right (n=10). (C) Knock-down of snx-6 cargo adaptor causes very long residence times of kiss & run vesicles. The RAB-5 wild-type vesicles are plotted as a dashed line for comparison (see Fig. S3A for single vesicle plots). Please note the elongated x-axis to accommodate vesicles with very long residence times (n=62). (D) Vesicles from snx-6 cargo adaptor knock-down worms show changes in size. RAB-5 vesicles were larger (wt: n=828, snx-6: n=1459) (see Fig. S3D for single worms). (E) HeLa cells were co-transfected with GFP-SNX1 and mApple-Rab5. Representative images from live cell imaging of ctr and snx5+6 KO are shown. Co-localization of Rab5 and SNX1 is increased in snx5+6 KO cells in comparison with the ctr cells. Furthermore, the structure of both Rab5 and SNX1 looks enlarged in snx5+6 KO cells in comparison with the ctr KO cells (n=3 independent experiments).

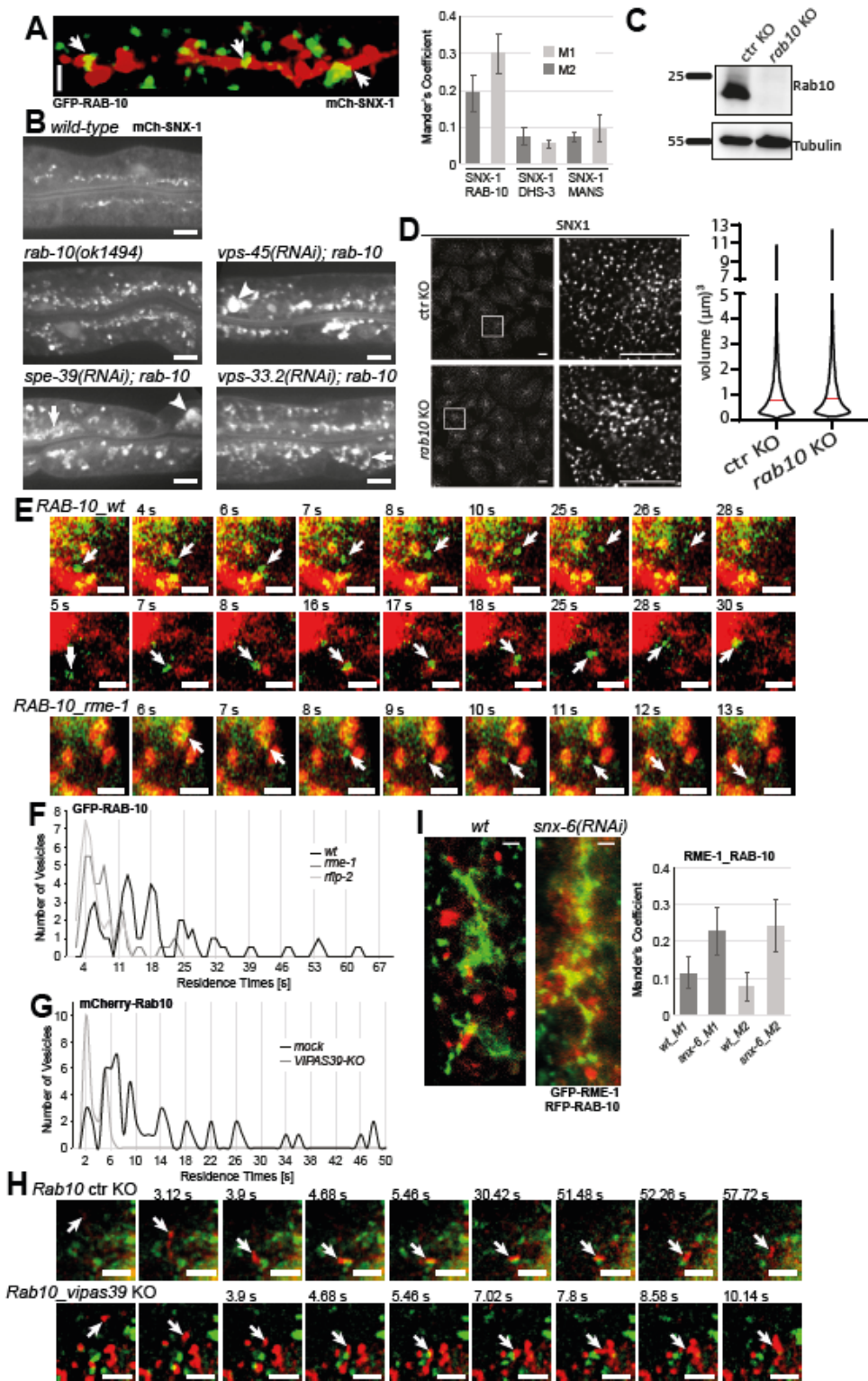


Figure 5

RAB-10 vesicles interact with SNX-1 compartments in similar ways as RAB-11 and RAB-5 vesicles. (A) GFP-RAB-10 compartments docking onto mCherry-SNX-1 networks (see also 3D projection Movie 7). Regions of co-localization are indicated by arrows. Quantification of co-localization by Mander's coefficients shows low but consistent overlap between RAB-10 and SNX-1, n=10. Scale bar: 2 μm . (B) Genetic interaction between FERARI subunits and RAB-10. Knock-out worm strain *rab-10(ok1494)* causes

accumulation of SNX-1 compartments, compared to wild-type. RNAi of *vps-45* and *spe-39* but not *vps-33.2* (CHEVI) show additional enlargement of SNX-1 (arrowheads). $n=20$ worms from 3 experiments. Scale bar: 10 μm . (C) Western blot data depicting the efficiencies of CRISPR-Cas9-mediated KO of *rab10* in HeLa cells ($n=3$ independent experiments). (D) Size of the endogenous SNX1 structure is enlarged in *rab10* KO cells. Antibodies against SNX1 were used to detect endogenous SNX1 by immunofluorescence. Violin plot showing the enlarged volume of the SNX1 structure in ctr and *rab10* KO cells (volume of more than 14,700 particles were measured from each group from three independent experiments, median is shown by the red stripe). (E) Movie stills for RAB-10 vesicles (arrow) showing kiss & run in *rme-1*(RNAi) and wild-type worms (Movie 8). (F) RAB-10 vesicles behave in very similar manner as RAB-5 vesicles, showing residence times with quantal increases ($n=51$). This behavior is abolished in *rme-1* ($n=40$) and *rifp-2* ($n=36$) knock-downs (Fig. S3B for single vesicle plots). (G) Kiss-and-run of Rab10 on sorting compartments is conserved in metazoans. Residence times of Rab10 vesicles exhibit characteristic intervals abolished in *vipas39*-KO cells (see Fig. S4G for single vesicle plots). (H) Movie stills for mCherry-tagged Rab10 vesicles (arrow) showing kiss-and-run on SNX1 (turbo-GFP-tagged) compartment in ctr KO and *vipas39*-KO HeLa cells ($n=3$ independent experiments, mock: $n=53$, *vipas39*-KO: $n=22$ vesicles) (see Movie 9). (I) Knock-down of cargo adaptor *snx-6* increases RFP-RAB-10 compartment co-localization with GFP-RME-1 FERARI member in *C. elegans*. Mander's coefficients are given on the right ($n=10$).

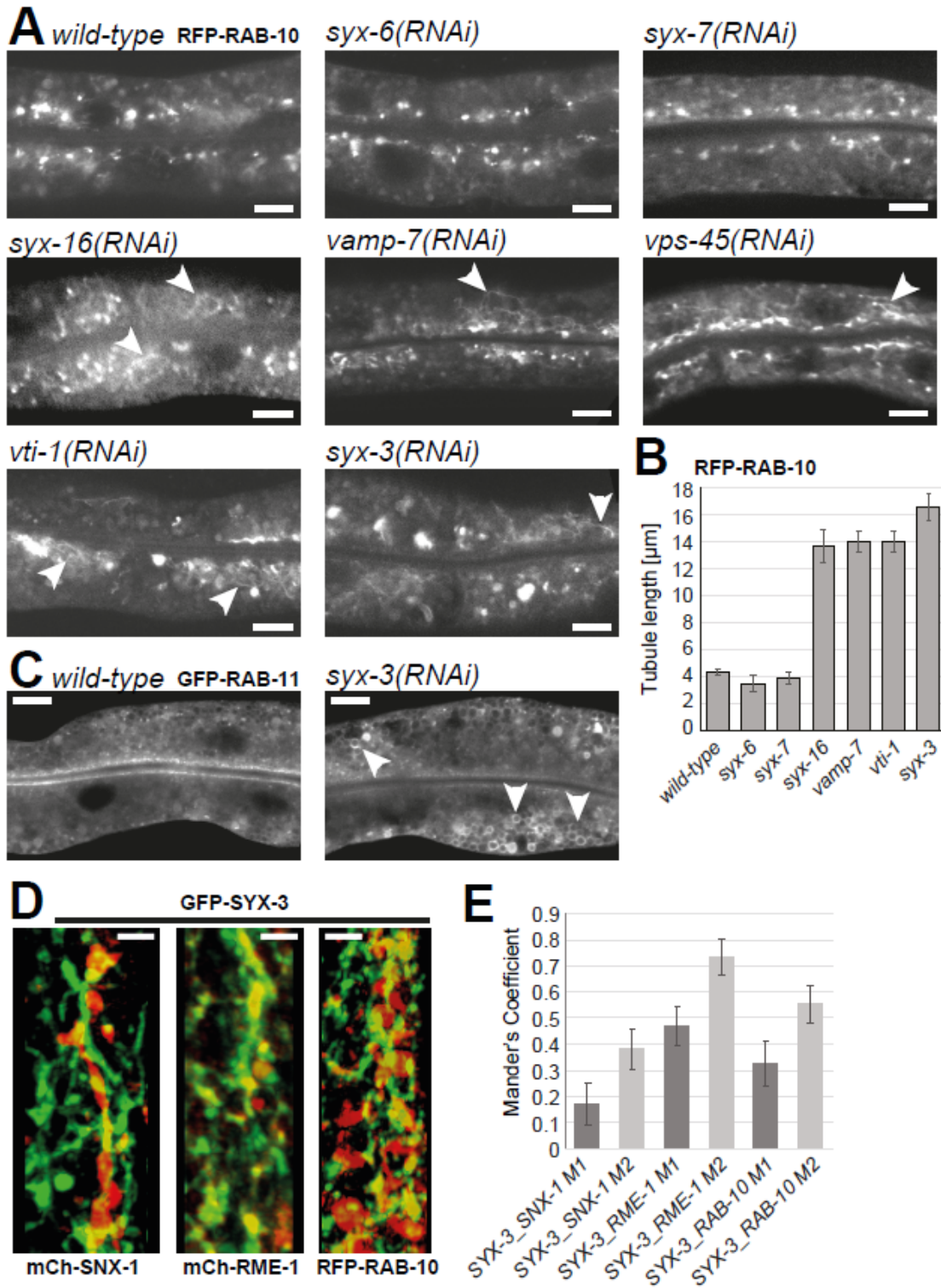


Figure 6

Specific SNAREs are used to dock RAB-10 vesicles through FERARI. (A) Knock-downs of *syx-16*, *vamp-7*, *vti-1* and *syx-3* cause FERARI-like phenotypes as seen in *vps-45(RNAi)* (long RFP-RAB-10 tubules indicated by arrowheads), while *syx-6* and *syx-7* do not. (B) Tubule length was quantified for 10 tubules in 6 worms each. (C) Knock-down of *syx-3* causes enlargement of RAB-11 compartments, similar to previously published FERARI knock-downs 7. (D) GFP-SYX-3 localizes to mCherry-SNX-1, mCherry-RME-1

and RFP-RAB-10 structures (Movie 10 with 3D projections). (E) Mander's coefficients are shown for n=10 worms.

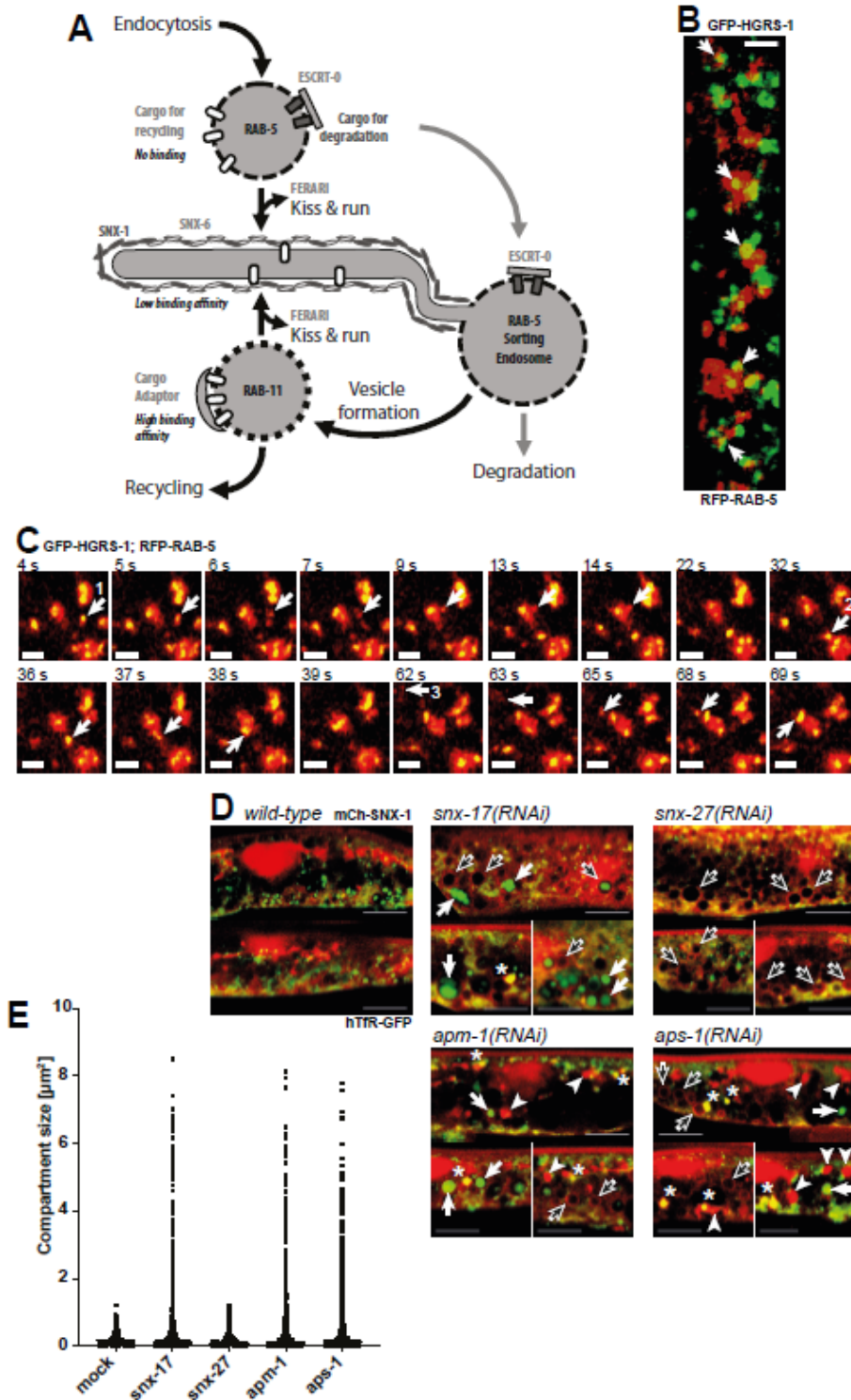


Figure 7

Effects of cargo adaptors on cargo flow (A) Cargo flow hypothesis, showing 3 subsequent steps of cargo sorting. First, RAB-5 vesicles unload non-bound recycling cargo and enrich ESCRT-bound cargo for transport into late endosomes/lysosomes. Second, low affinity binding to SNX-6 organizes cargo inside

the SNX-1 tubular network. Third, higher affinity adaptors in RAB-11 vesicles are used to bind cargo for final transport to destination (e.g. plasma membrane). Subsequent steps of kiss & run ensure enrichment of wanted cargoes (and loss of unwanted ones), allowing for a “proofreading” of cargo content despite low binding affinities to adaptors. (B) ESCRT-0 subunit HGRS-1 can frequently be found on RAB-5 compartments (arrows) (3D projection in Movie 11). (C) Cargo for degradation can potentially be retained on moving RAB-5 vesicles by the presence of ESCRT-0 subunit HGRS-1. Movie stills showing 3 RFP-RAB-5 vesicles fusing with a larger sorting endosome (homotypic fusion). Vesicles contain GFP-HGRS-1 domains and move with similar dynamics as small RAB-5 vesicles that perform kiss & run (see Movie 12). (D) Adaptor knock-downs affect cargo traffic through SNX-1 compartments. RNAi of *snx-17*, *snx-27*, *apm-1* or *aps-1* cause enlargement of SNX-1 compartments (black arrows: large empty round compartments, arrowheads: large filled compartments (see also Fig. S5D)). The model cargo hTfR-GFP was found in enlarged compartments as well (white arrows). These accumulations were absent in *snx-27*(RNAi) worms. Some of the hTfR accumulations co-localized with enlarged SNX-1 structures (asterisks). (E) Quantification of enlarged hTfR-GFP compartments in adaptor knock-down worms (n=6).

Supplementary Files

This is a list of supplementary files associated with this preprint. Click to download.

- [SupplFig1.ai](#)
- [SupplFig2.ai](#)
- [SupplFig3.pdf](#)
- [SupplFig4.ai](#)
- [SupplFig5.ai](#)
- [SupplFig6.ai](#)
- [TableS1.docx](#)
- [Movie1RAB11snx6.mp4](#)
- [MovieS1RAB7worms.mp4](#)
- [Movie2Rab11HeLa.mp4](#)
- [Movie3RAB5worms.mp4](#)
- [Movie4Rab5HeLa.mp4](#)
- [Movie5RAB5homworms.mp4](#)
- [Movie6RAB5snx6.mp4](#)
- [Movie7RAB10.mp4](#)
- [Movie8RAB10worms.mp4](#)
- [Movie9Rab10HeLa.mp4](#)
- [Movie10SYX3.mp4](#)

- [Movie11HGRS1.mp4](#)
- [Movie12HGRS1worms.mp4](#)